

From Zero to High-Speed Racing: An Autonomous Racing Stack

Hassan Jardali, Durgakant Pushp, Youwei Yu, Mahmoud Ali, Ihab S. Mohamed, Alejandro Murillo-Gonzalez, Paul D. Coen, Md. Al-Masrur Khan, Reddy Charan Pulivendula, Saeoul Park, Lingchuan Zhou, and Lantao Liu

Luddy School of Informatics, Computing, and Engineering at Indiana University, Bloomington.

Abstract. High-speed, head-to-head autonomous racing presents substantial technical and logistical challenges, including precise localization, rapid perception, dynamic planning, and real-time control—compounded by limited track access and costly hardware. This paper introduces the Autonomous Race Stack (ARS), developed by the IU Luddy Autonomous Racing team for the Indy Autonomous Challenge (IAC). We present three iterations of our ARS, each validated on different tracks and achieving speeds up to 260 km/h. Our contributions include: (i) the modular architecture and evolution of the ARS across ARS1, ARS2, and ARS3; (ii) a detailed performance evaluation that contrasts control, perception, and estimation across oval and road-course environments; and (iii) the release of a high-speed, multi-sensor dataset collected from oval and road-course tracks. Our findings highlight the unique challenges and insights from real-world high-speed full-scale autonomous racing.

1 Introduction

Developing large-scale autonomous systems, particularly those highlighted by competitions such as the DARPA Challenges, faces considerable technical and logistical challenges. High-speed autonomous racing exemplifies these difficulties, as it demands precise localization, rapid perception, and real-time planning and control under extreme dynamic conditions. However, significant hardware investment and limited track time restrict development, making well-planned real-world tests crucial. This paper describes the development of the Autonomous Race Stack (ARS) by our team for participation in the IAC, presenting its iterative evolution, the rationale behind key design choices, and performance insights from real-world testing on both oval and road-course tracks. More precisely, this paper details the development and evaluation of three successive ARS iterations: ARS1, validated at the Indianapolis Motor Speedway (IMS) at speeds up to 205 km/h; ARS2, demonstrated at the Las Vegas Motor Speedway (LVMS) reaching 260 km/h, and later tested on the Las Vegas Road Course (LVRC); and ARS3, designed for head-to-head autonomous racing on road-course tracks and partially validated at both LVMS and LVRC. We discuss the evolution of the stack across these iterations, highlighting key architectural updates, technical challenges, and insights gained through real-world testing.

The initial version, ARS1, incorporates filter-based state estimation fusing Global Navigation Satellite System (GNSS) and inertial measurements, and employs a Pure Pursuit controller to track racelines generated via the minimum curvature method [1]. Building on this foundation, ARS2 introduces multi-vehicle capabilities, including radar-based perception, Adaptive Cruise Control (ACC), and an Anti-lock Braking System



Fig. 1: IU-Luddy's IAC AV24 racing vehicle at LVMS.

(ABS), while also utilizing a linear Model Predictive Controller (MPC) for lateral control. The latest iteration, ARS3, integrates exteroceptive sensor data into an optimization-based state estimation framework [2], enhances opponent reasoning through coupled radar and LiDAR perception, and features an integrated stochastic MPC for combined longitudinal and lateral control.

Numerous teams have participated in the IAC, each developing its own full-scale autonomous racing stack, with several prior works [3–5] demonstrating impressive performance on the Dallara AV21, the IAC’s previous-generation autonomous vehicle. This work distinguishes itself by documenting the systematic evolution of our software across three iterations, providing a detailed performance analysis on both oval and road-course tracks—thereby expanding the scope beyond predominantly oval-focused studies. Additionally, we analyze a spin incident recorded at LVRC. We build on these advancements to make the following contributions:

1. **Autonomous Race Stack:** We introduce a comprehensive ARS designed for solo and multi-vehicle racing on both oval and road-course tracks, validated on a full-scale IAC AV24 platform, as shown in Fig. 1. The system has demonstrated stable performance at speeds reaching up to 260 km/h.
2. **Evaluation:** We present a performance evaluation of each ARS subsystem, supplemented by analytical justifications and insights into our system updates.
3. **Dataset:** We provide high-speed sensor data collected from the IMS, LVMS, and LVRC tracks, highlighting the significant challenges of synchronizing and fusing information from cameras, radars, and LiDARs to achieve reliable localization, dynamics estimation, and opponent detection*.

2 System Architecture

In this section, we introduce the IAC AV24 vehicle and then our software architecture.

2.1 Hardware Architecture

The IAC AV24 race car is based on the Dallara IL15 design and equipped with a 2 L single-turbo inline-4 engine with 488 HP. Its cockpit is replaced by autonomous components, including a dSPACE Autera AutoBox with an Intel Xeon 3GHz 12-core CPU and an NVIDIA A5000 GPU. It runs Ubuntu 22.04 with ROS2 Humble and Cyclone DDS as a middleware for real-time communication and core development framework. The equipped sensors related to critical autonomy modules are as following:

- Three Luminar Iris LiDARs operating at 10 Hz;
- Six Mako G-319C cameras with a resolution of 2064×1544 at 10 Hz;
- Two Continental ARS548 4D Radars at 20 Hz;
- Two NovAtel PwrPak7D GNSS units (Top and Side) at 20 Hz with IMUs at 125 Hz;
- One VectorNav-310 GNSS unit at 5 Hz with IMU at 200 Hz.

This diverse sensor configuration enables robust state estimation and perception, supporting the vehicle’s operation across both oval and road-course racing environments.

2.2 Autonomy Stack Overview

Building on the hardware capabilities of the IAC AV24 autonomous race car, our autonomy stack integrates multiple high-performance modules to enable safe and competitive racing.

*See <https://iu-vail.github.io/IU-ARS> for access to the open-source data and dashboard code.

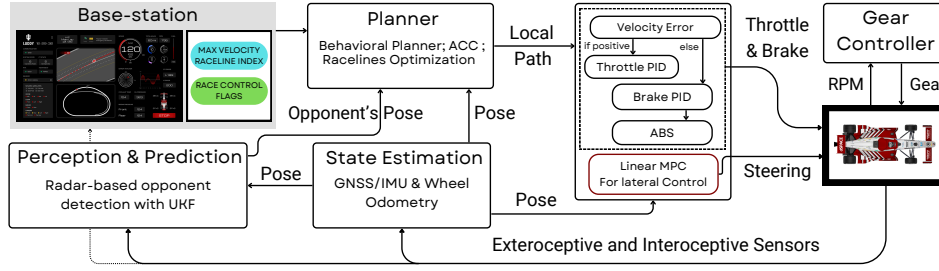


Fig. 2: System architecture of ARS2 with core modules' details.

The vehicle operates on both oval and road-course tracks under two primary race formats: a solo-vehicle (SV) format, defined as a time trial where a single car records its fastest lap time, and a head-to-head (H2H) format that includes two cars on non-intersecting lines. The autonomy stack is composed of several interconnected modules. A state estimation module fuses measurements from multiple onboard sensors to estimate the ego vehicle's pose and velocity. This is complemented by a perception and prediction system responsible for detecting nearby opponents and forecasting their future trajectories. Based on this situational awareness, a behavioral planner determines whether to maintain a distance with the leading car or initiate an overtaking maneuver. A path planner then generates dynamically feasible trajectories, which are followed by a control module that issues low-level actuation commands: steering for lateral control, and throttle, brake, and gear shifting for longitudinal control. A remote base-station interface enables real-time monitoring of system status and performance, while also allowing the operator to issue race-time parameters such as maximum target speed. The dashboard for live data visualization was continuously updated in line with stack revisions. The complete ARS2 system architecture is shown in Fig. 2.

Table 1: Key architectural differences between ARS1, ARS2, and ARS3.

Feature	ARS1	ARS2	ARS3
Racing Scenario	SV	SV & H2H	SV & H2H
Track	IMS	LVMS & LVRC	LVMS & LVRC
Top Speed	205 km/h	260 km/h (LVMS) 195 km/h (LVRC)	72 km/h (both)
Estimation	GPS/INS	ARS1 & Wheel Odometry	ARS2 & LiDAR
Perception	N/A	Radar	Radar & LiDAR
Lateral Controller	PP	MPC	MPPI

3 Evolution of the IU-Luddy Autonomous Racing Stack

In this section, we describe the evolution of our software stack across its three iterations by detailing the key updates within each module. Additionally, the differences between iterations are highlighted in Table 1.

3.1 ARS1: Time Trials

ARS1, the initial iteration of our autonomous racing stack focused on single-vehicle racing, was validated at IMS in September 2024. The primary design goal was to create a system that is both minimally complex and inherently stable. The *state estimation* module employs an error-state extended Kalman filter (ESKF), fusing NovAtel-Top GNSS with both NovAtels' inertial data via Manifold [6]. The ESKF propagates the state $x \in \mathbb{R}^{18}$, includ-

ing position ($\in \mathbb{R}^3$), velocity ($\in \mathbb{R}^3$), orientation ($\in \mathbb{R}^3$), and their first-order derivatives. The *planning module* generates a global raceline offline using the minimum curvature method [1], while the online planner outputs the nearest path segment in the car's frame. *Control* is achieved via a Pure Pursuit (PP) steering controller, which computes the steering angle δ using the geometric relation: $\delta = \arctan(2L \sin \alpha / L_{fw})$, where L is the vehicle wheelbase, α is the heading angle to the target point on the path, and L_{fw} is the adaptive look-ahead distance determined by the current vehicle velocity v_{car} . This is coupled with a PID-based longitudinal controller, where the velocity error $e_v = v_{target} - v_{car}$, with $v_{target} = \max(v_{max}, v_{raceline})$, governs PID activation: the throttle PID is used if $e_v > 0$, and the brake PID is triggered if $e_v < -\kappa_{db} v_{target}$, where κ_{db} is a deadband coefficient. Gear shifting is regulated based on engine RPM.

3.2 ARS2: Toward Multi-Agent Racing via Advanced Planning and Control

ARS2 extends the capabilities of ARS1, introducing enhancements to the state estimation and control modules and incorporating new components essential for multi-vehicle racing. These additions include a perception module for opponent detection, a prediction module, a behavioral planner, and adaptive cruise control. This version was validated on LVMS and LVRC in January and April 2025, respectively.

The *state estimation* module in ARS2 augments the existing ESKF with vehicle dynamics odometry. To preserve the accuracy of the yaw angle estimation, roll and pitch angles are estimated independently. The vehicle single-track model incorporates wheel speed and steering angle measurements to refine the state's velocity. We smooth the inconsistency caused by possibly long-term wheel odometry dead-reckoning via an inverse multi-quadratic (IMQ) weighting function [7], denoted as $w(x_t, \hat{x}_t) = (1 + \|x_t - \hat{x}_t\|_2^2 / c^2)^{-1/2}$, with the soft threshold c , the predicted robot state \hat{x} , and the measurement x . IMQ is applied to the Kalman gain K , thereby influencing the update of state covariance Σ :

$$\Sigma_t^{-1} \leftarrow \Sigma_{t|t-1}^{-1} + w_t^2 H_t^\top R_t^{-1} H_t, \quad K_t \leftarrow w_t^2 \Sigma_t H_t^\top R_t^{-1},$$

with measurement matrix H_t and its noise covariance R_t . Additionally, we create a safety state machine so that the supplementary NovAtel-Side (i.e., with antennas on two sides) will take over if the main NovAtel-Top loses signals for 0.5 s.

For *perception*, ARS2 employs a radar-based *opponent detection* algorithm. The choice of radar over LiDAR for this task stems from its capacity for direct velocity measurement, its higher update rate, and its lower computational load. The radar outputs a 4D point cloud $P = \{p_i\}_{i=1}^N$, where each point p_i is defined by its Cartesian coordinates and radial velocity, along with multiple signal quality metrics. An initial filtering step is applied using predefined thresholds for these metrics, including signal-to-noise ratio (SNR), existence probability, peak detection confidence, received signal strength (RSS), and ambiguity identification. Subsequently, static objects—identified by radial velocities matching the negative of the ego-car velocity—are filtered out. The remaining dynamic objects are then clustered based on their 3D spatial coordinates and radial velocity using the DBSCAN algorithm [8]. A valid cluster C is retained only if it contains at least N_{min} points, increasing robustness against noise. Clusters undergo a coordinate transformation from the ego-vehicle's radar frame to the global frame, then filtered using the track boundary as follow $p_i \in \Omega_{outer} \setminus \Omega_{inner}$, where Ω_{outer} and Ω_{inner} denote the outer and inner track boundaries set, respectively. This step efficiently filters out clusters outside the track caused by radar multipathing. Fig. 3 shows a radar observation, illustrating both the opponent vehicle

and multipath reflections, with point color representing radial velocity. A cost function is computed between the current opponent detections at time-step k and the prior estimate at $k - 1$, incorporating both the opponent's 3D pose and velocity. The detection with the minimal cost is then propagated to an Unscented Kalman Filter (UKF) [9], that employs a point-mass motion model, for robust *opponent tracking*. This approach ensures reliable opponent tracking, even in scenarios where detections are temporarily unavailable. In multi-vehicle scenarios within ARS2, participating vehicles typically operate on parallel race-lines to ensure safety. The *behavioral planning* module processes opponent detection data from the perception module to make high-level strategic decisions. It selects between two primary operational modes: *Follow mode* or *Attack mode*, with the choice contingent upon inputs from race control and adherence to competition regulations.

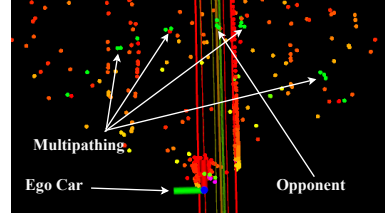


Fig. 3: Front Radar Pointcloud.

In the Follow mode, an ACC system is employed. The ACC dynamically modulates the ego vehicle's longitudinal speed to maintain a predefined, safe separation distance from the leading vehicle. Conversely, activation of the Attack mode authorizes the ego vehicle to accelerate, thereby initiating an overtaking maneuver. The ACC system calculates a preliminary desired longitudinal velocity, v'_{des} , for the ego vehicle. This calculation considers the state of both the ego and leading vehicles, and is given by: $v'_{des} = v_l + K_d (d - (d_0 + \max(0, \tau_{des}(v_e - v_l))))$ where v'_{des} is the preliminary desired longitudinal velocity, v_l is the leading vehicle's velocity, v_e is the ego vehicle's velocity, d is the longitudinal separation, d_0 is the target separation distance, τ_{des} is the desired inter-vehicle time gap, and K_d is a gain parameter.

For *longitudinal control*, an ABS was implemented for road-course racing; it operates by continuously calculating the slip ratio for each wheel—defined as the normalized difference between the vehicle's longitudinal speed and the wheel's tangential speed, $\lambda = (V_{veh} - \omega R)/V_{veh}$ and then employs a PID controller to regulate brake pressure and track the optimal slip ratio, thereby preventing wheel lock-up and maximizing deceleration. By avoiding lock-up during aggressive deceleration, particularly before turns, ABS maintains optimal tire traction. This enhances braking effectiveness, preserves steerability to mitigate understeer, and improves vehicle stability, ultimately reducing the risk of spinning. With respect to *lateral control*, ARS2 employs a linear Model Predictive Control (LMPC) framework. The controller is formulated based on the lateral single-track dynamic model described in [10] and explicitly accounts for road banking angles, which can reach up to 20° at LVMS. The LMPC is implemented using the ACADOS optimization package [11].

3.3 ARS3: LiDAR-Based Odometry, Perception, and Stochastic Control

ARS3 represents the latest proposed iteration of our autonomous racing software stack, featuring significant advancements in key areas such as an enhanced LiDAR-based state estimation and perception modules, alongside the implementation of a stochastic sampling-based controller, specifically a Model Predictive Path Integral (MPPI) controller [12]. While ARS3 has been deployed and subjected to initial testing at LVRC, full integration and validation of all updated modules were constrained by limited track access and debugging windows.

In ARS3, we aim to improve the *state estimation* accuracy by tightly coupling the rich sensor suite through nonlinear incremental optimization, specifically iSAM2 [2], where its chordal Bayes tree structure can leverage diverse sensory inputs. To improve the robustness of simultaneous localization and mapping (SLAM), we leverage RTK to construct point-cloud maps offline, which are subsequently used as priors for LiDAR registration [13]. Three LiDAR sensors operate asynchronously to enhance state estimation, particularly in orientation. Moreover, they serve as the primary source of state estimation when all GNSS devices become unavailable. For the *perception* module, ARS3 leverages LiDAR to overcome key limitations of radar, enhancing the detection of static obstacles on the track, such as vehicles halted due to safety checks. For *control*, the architecture features a GPU-accelerated MPPI controller as the primary mechanism for generating longitudinal acceleration and steering commands [14]. It was initially tested with the kinematic bicycle model, where a PID controller was used to convert longitudinal acceleration into throttle and brake signals. In the updated version, the controller employs a single-track dynamic model that directly outputs throttle, brake and throttle commands.

4 Experiments

This section presents a series of experiments conducted to evaluate the successive iterations of our autonomous racing software stack. We report results from deployments of ARS1 at the IMS in September 2024, ARS2 at LVMS in January 2025 and LVRC in April 2025. Preliminary results for ARS3 are also included at the end of this section.

4.1 State Estimation

We evaluate the localization performance using running statistics. Rather than relying on RTK as ground truth, we assess the satellite navigation (satnav)-inertial fusion during the ARS1 deployment and the dynamics-satnav-inertial fusion during ARS2. Our metrics include heading and position jerks, defined as the third derivative of the heading and position over time. During ARS1, our satnav-inertial system achieves a heading jerk of $407.6^\circ/\text{s}^3$ and a position jerk of $1387.17\text{ m}/\text{s}^3$. In ARS2, our dynamics-satnav-inertial fusion improves these to $305.56^\circ/\text{s}^3$ and $774.16\text{ m}/\text{s}^3$, benefiting from the vehicle dynamics odometry based on the single-track model for enhanced consistency and robustness. Since the same controller was used for all localization tests, these motion stability metrics directly reflect the improvements in localization. Moreover, as shown in Fig. 4, the pointcloud overlapped with the LVMS map validates the scale consistency. Note that the pointcloud is projected solely based on dynamics-satnav-inertial fusion without any LiDAR odometry.

During testing at LVRC, we experienced no RTK dropouts exceeding 0.5 s. Nonetheless, to assess the robustness of our localization system, we intentionally disabled the GPS, resulting in no sensor outputs. As shown in Fig. 4, the system exhibited a maximum deviation of approximately 0.5 m after 6 seconds of GPS denial on both straight segments and turns. The recovery to nominal pose was smoothly managed by the IMQ mechanism. In terms of IMQ parameters, we use a vehicle speed-based soft threshold c . Position uses $\max(0.75, \min(3, v \cdot \Delta t))$ and orientation uses $\max(\frac{\pi}{36}, \min(\frac{\pi}{18}, \omega \cdot \Delta t))$ with linear speed v [m/s] and angular velocity ω [rad/s].

4.2 Perception and Prediction

In ARS1, we collected initial data involving an opponent vehicle. Using this data, the radar-based opponent detection and tracking algorithm was evaluated offline to verify its functionality and real-time performance. Subsequently, in ARS2, this algorithm was

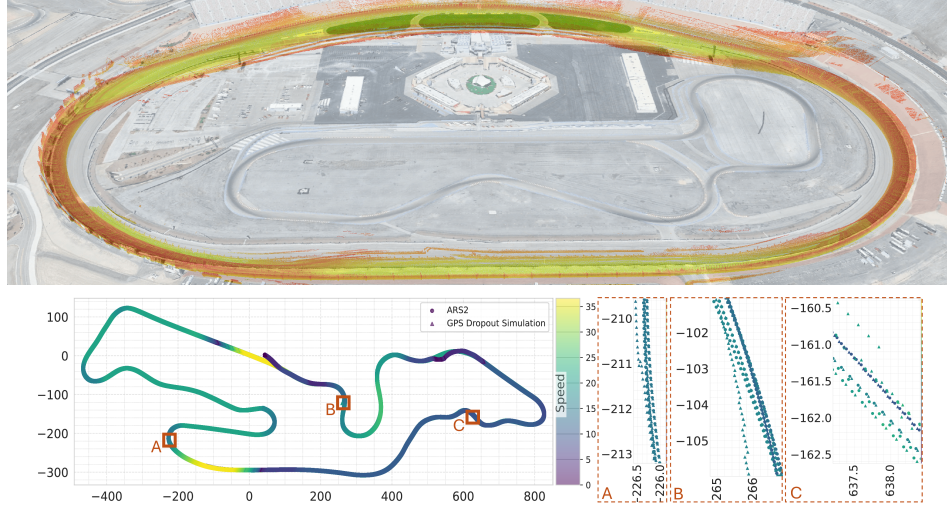


Fig. 4: (Top) Pointcloud mapping at LVMS with poses estimated by dynamics-satnav-inertial fusion. (Bottom) GPS dropout simulations on track with zoomed-in view.

tested on-track at LVMS during practice sessions involving two autonomous vehicles, monitored by the IAC chase car, where the opponent vehicle maintained varying speeds and relative distances from the ego vehicle. The algorithm operated reliably at a frequency of 20 Hz, consistently detecting opponents at distances of up to 200 m across a range of speeds between 7 m/s and 28 m/s. The ARS2 detection algorithm demonstrated robust performance under dynamic conditions, with an opponent velocity error of -0.007 ± 1.35 m/s and a distance error of 0.82 ± 0.91 m (see Fig. 5a and Fig. 5b). The radar-based opponent detection was further improved through two key modifications: (i) the addition of a logic to detect when the opponent car is stopping based on its velocity and acceleration, and (ii) the application of a moving average filter to smooth the opponent's estimated velocity. This enhanced estimation was validated during testing at LVRC (Figs. 5c and 5d), resulting in reduced errors in velocity (0.05 ± 0.53 m/s) and mean distance error (0.67 ± 1.76 m) compared to earlier results at LVMS. While the standard deviation of velocity error showed particular improvement, the distance standard deviation was larger due to one big jump that occurred before the hairpin (see Fig. 6). However, gaps in detection were observed at LVRC due to the radar's limited field of view (FoV). These gaps occurred when either the ego vehicle or the opponent entered or exited a sharp curve, causing the opponent to fall outside the radar FoV (see highlighted yellow circles in Fig. 6).

4.3 Planning and Control

In ARS1, our autonomous racing vehicle achieved a maximum speed of 205 km/h while using Pure Pursuit (PP) for steering control. The cross-track error (i.e., lateral deviation from the pre-planned raceline) ranged from -1.5 m to 0.6 m, while the heading error (i.e., deviation from the raceline heading at the closest point) varied between -2.0° and 2.25° . While the vehicle remained stable throughout operation, oscillations were observed. The maximum lateral acceleration, a critical factor for vehicle dynamics and tire limits, reached 18 m/s^2 . In contrast, longitudinal acceleration was negligible on ovals due to constant high speeds. In ARS2, lateral control was enhanced using an MPC based on the single-track

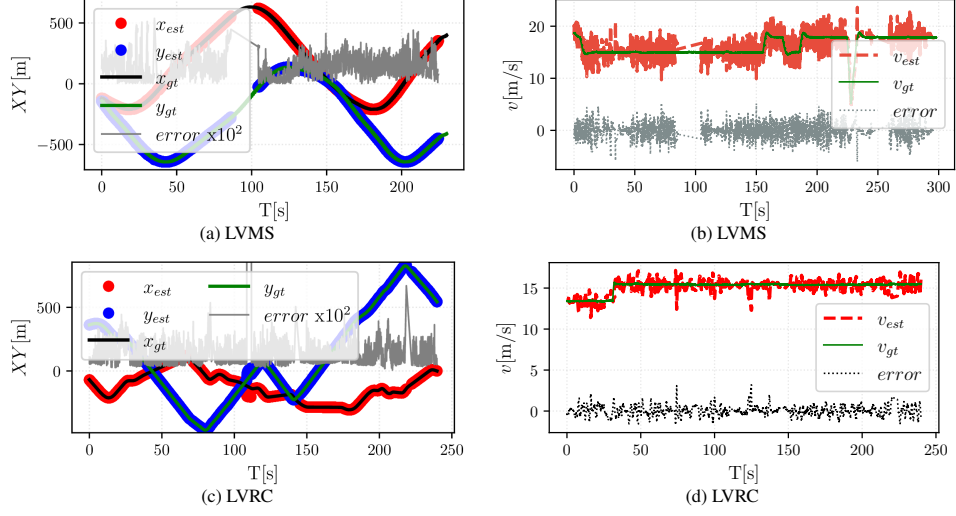


Fig. 5: Comparison of estimated and ground-truth opponent states: (a) and (c) depict the UKF-estimated XY position (x_{est} , y_{est}) alongside the ground truth (x_{gt} , y_{gt}) from shared opponent localization, where the position error is defined as the Euclidean distance between them and scaled by a factor of 100 for clarity; (b) and (d) present the estimated velocity (v_{est}) versus the ground truth (v_{gt}), along with the absolute velocity error.

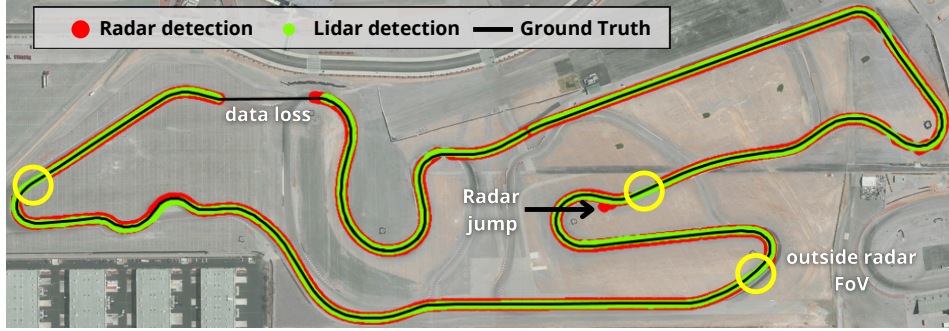


Fig. 6: Opponent Tracking: radar-based tracking during the LVRC testing (running on our vehicle), while LiDAR-based tracking was tested on the recorded bag files.

dynamic model with banking compensation [10]. This achieved a maximum speed of 260 km/h, with a cross-track error between -1.6 m and -0.4 m and a heading error within $\pm 1^\circ$. Maximum lateral acceleration increased to 28 m/s^2 . At LVRC, a road-course track, the vehicle's behavior differed significantly from that on ovals. Specifically, cross-track error ranged from -0.6 m to 0.5 m, and heading error varied within $\pm 4^\circ$ at a maximum speed of 191 km/h. The performance of both controllers, in terms of cross-track error versus velocity during high-speed runs on all three tracks, is depicted in Fig. 7a. Racing on the road course inherently involves dynamic changes in acceleration. The vehicle experienced varying lateral accelerations from alternating turns, reaching a peak magnitude of 10 m/s^2 . Longitudinally, the vehicle consistently switched between accelerating and braking, which resulted in a peak deceleration of -15 m/s^2 . The differences in acceleration behavior between ovals and road-course tracks can be seen in Fig. 7b.

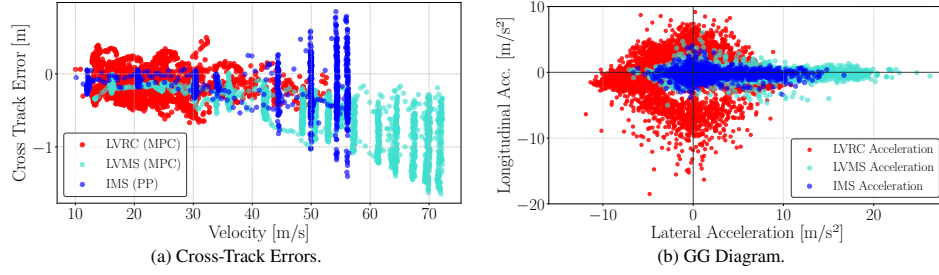


Fig. 7: MPC and PP controllers performance on oval (IMS, LVMS) and road-course (LVRC) tracks: (a) trajectory tracking vs velocity and (b) lateral–longitudinal acceleration (GG diagram).

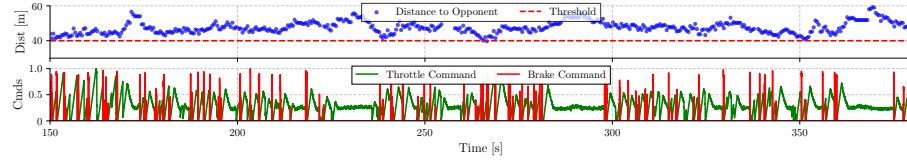


Fig. 8: ACC performance showing curvilinear distance to the opponent (top) and the resulting normalized control commands (bottom).

The ACC was validated during testing at LVRC. Its effective operation is demonstrated in Fig. 8, which illustrates brake activation as the curvilinear distance to a leading vehicle decreased to the predefined safety thresholds. In the depicted scenario, the vehicle was initially commanded to maintain a constant velocity of 60 km/h. Subsequently, as the lead vehicle was detected and the gap reduced, the ACC system appropriately commanded a lower velocity. As a result, the longitudinal controller successfully tracked this updated setpoint from the ACC, actuating the brakes to ensure a safe following distance.

A critical instability event was observed during ABS evaluation on our final practice day at LVRC. The sequence initiated when the vehicle commenced deceleration for an upcoming turn. However, due to suboptimal tuning, the ABS failed to deliver the commanded deceleration, causing the vehicle to approach the turn entry at a velocity significantly higher than intended. This excessive entry speed led to pronounced understeer. In this condition, the front tires exceeded their capacity for lateral grip before the rear tires, resulting in the vehicle’s trajectory becoming wider than that dictated by the steering input; essentially, the vehicle deviates outward from the desired cornering arc. Simultaneously, slip angles, defined as the angle between the direction a tire is pointing and its actual direction of travel, began to increase, particularly at the front axle. It is crucial to distinguish slip angles, which are primarily associated with *lateral force* generation during cornering, from slip ratios, which are associated with *longitudinal forces*. While the initial failure involved ABS performance related to slip ratios (blue area in Fig. 9), the subsequent loss of control was characterized by excessive slip angles (red area in Fig. 9). Concurrently, two factors exacerbated the situation. First, as the vehicle’s speed decreased, the gear controller, unaware of the high slip angles and the demanding high-curvature maneuver, commanded a downshift, causing high slip ratios at the rear tires. Second, the lateral MPC, attempting to correct the increasing cross-track error caused by understeer, commanded a progressively larger steering angle. The combination of these events led to a rapid increase in tire slip angles, indicating the onset of a spin. Ultimately, the high steering command, coupled

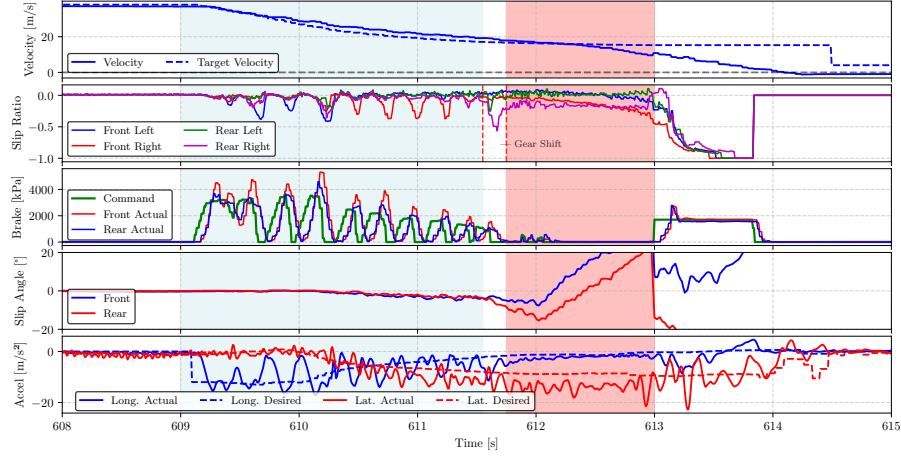


Fig. 9: Vehicle data during an ABS-induced spin event. The plots display: Vehicle and target velocities, tire slip ratios, commanded versus actual brake pressures, estimated slip angles [10], and target and IMU-measured actual accelerations. Blue shaded regions indicate ABS activation, while red shaded regions denote the vehicle spin. An increase in rear axle slip ratio is observed during gear shifting. Lastly, a safety check activated the brakes.

with the vehicle’s compromised state, resulted in a complete spin. A video of this incident is provided in the supplementary material for further analysis.

4.4 Preliminary Testing Results of ARS3

Different from ARS2 which was fully validated on the vehicle, certain new components of ARS3’s such as the LiDAR methods were validated only using offline data at the current stage, due to the limited access to tracks and vehicles in this racing season. For *state estimation*, LiDAR odometry computation time recorded 0.1 ± 0.06 s per frame on a Intel i9-14900KF CPU with four threads allocated. The results show better yaw angle accuracy, contributing to improved safety. Previously, GPS-based estimation caused up to three yaw jumps per lap, each reaching approximately 2° . With LiDAR, the yaw angles remain consistent throughout the lap, and the resulting map shows visually stable track boundaries, indicating reliable pose estimation. For *perception*, the LiDAR-based opponent tracking system was validated on recorded bag files, demonstrating a mean pose error of 1.89 ± 1.59 m/s and a mean velocity error of 0.49 ± 1.50 m/s. However, real-time deployment on the vehicle’s onboard computer, while running all modules concurrently, introduced latency exceeding 1 second. For *control*, the MPPI controller was tested on track using a kinematic model at LVMS, achieving a speed of 72 km/h, and similarly tested at LVRC with comparable speeds. However, due to limited time for tuning, the performance was not sufficient to safely increase the speed further. Improving the performance of this new controller is our next goal.

5 Experimental Insights

We also present key insights and discussions based on our experimental results.

5.1 State Estimation with Redundant Sensors

As introduced in Section 2, each sensor has its backups, but inconsistent extrinsic calibrations pose a significant challenge for sensor fusion. Common practices rely on supple-

mentary sensor motion measurements to enhance motion estimation accuracy; however, this approach restricts pose transitions between sensors at high vehicle speeds when the primary sensor fails (e.g., due to hardware connection loss). Regarding transitions between different GNSS devices, we mainly rely on IMQ smoothing to avoid sudden jumps. We will investigate a consistent transition algorithm for high-speed situations. Moreover, exteroceptive sensor (e.g., LiDAR, camera) odometry [13, 15] typically suffers from scale ambiguities, further complicating sensor transitions. While coupling sensors can improve accuracy under normal conditions, we will investigate methods to ensure safe and smooth transitions in ARS3. Here, safety refers to solution ambiguity, i.e., when the loss function converges but the solution is unrealistic. We plan to explore cross-validation techniques, including versatile feature selection online and map tracking with different sensors.

5.2 Perception Hallucinations

False-positive detections typically arise from environmental factors such as multipath radar signals or sensor noise, potentially causing unintended behavior within the planning module. In ARS2, track boundaries and historical detection data were utilized to mitigate these false detections. Unlike radar, LiDAR is not susceptible to multipath effects, suggesting that LiDAR-radar fusion could significantly reduce false positives and improve perception reliability. As demonstrated in Fig. 6, the LiDAR-based tracking component effectively compensates for radar FoV limitations (highlighted in yellow circles) while eliminating radar tracking discontinuities caused by radar multipath interference. The current LiDAR-based tracking system could not be deployed in real-time due to computational constraints—execution times exceeded 1 s. Future work will focus on optimizing computational efficiency to enable real-time fused LiDAR-radar tracking.

5.3 Planning-Control Framework

In ARS2, the planning architecture integrates an *offline-generated optimal raceline* with an *online module*. The online component encompasses a *behavioral planner* for multi-vehicle interactions, tailoring its decisions based on competition rules, and an ACC system. For high-speed multi-vehicle racing scenarios on road-courses, a *local motion planner* is needed within this online framework to generate dynamically feasible trajectories for overtaking maneuvers as the assumption that both cars travel on parallel racelines is not always valid. The control system employs a decoupled approach. *Longitudinal control* is achieved using two PID controllers, one for throttle and another for braking, complemented by an ABS designed to maximize deceleration. For *lateral control*, a linear MPC is implemented. While this decoupled strategy has proven effective in many scenarios, it has inherent disadvantages that can, under certain conditions, lead to vehicle instability, as demonstrated by the spin incident shown in Fig. 9 at LVRC. Our future efforts therefore include tuning the coupled MPPI controller that considers nonlinear vehicle dynamics.

5.4 Conclusion and Future Work

This paper has presented performance results for the ARS1 and ARS2 systems on both oval tracks and road courses. The development and comprehensive validation of our subsequent system, ARS3, encountered practical limitations, primarily restricted track access and computational constraints. Future work will therefore be directed towards overcoming these challenges and enhancing ARS3's capabilities. Key areas of focus will include addressing computational issues through the optimization of sensor drivers and further refining the vehicle dynamics model along with the MPPI controller parameters. Additionally, efforts are

being directed towards improving the precision of opponent vehicle trajectory prediction and advancing the local planner's ability to generate overtaking maneuvers effectively.

6 Acknowledgement

We acknowledge support from NSF Grants #2047169, #2006886, and the IU Luddy Autonomous Racing Initiative for funding related robotics research and racing event travel. Paul D. Coen was supported by the NISE/PhD Fellowship at NSWC Crane during his participation in 2024. We thank Shaekh Shithil and Paul O. Quigley for their assistance with racing experiments, and we are grateful to the technical and logistics personnel of the Indy Autonomous Challenge for their support.

References

1. A. Heilmeier, A. Wischnewski, L. Hermansdorfer, J. Betz, M. Lienkamp, and B. Lohmann, "Minimum curvature trajectory planning and control for an autonomous race car," *Veh. Syst. Dyn.*, 2020.
2. M. Kaess, H. Johannsson, R. Roberts, V. Ila, J. Leonard, and F. Dellaert, "iSAM2: Incremental smoothing and mapping with fluid relinearization and incremental variable reordering," in *2011 IEEE International Conference on Robotics and Automation*, 2011, pp. 3281–3288.
3. A. Raji, D. Caporale, F. Gatti, A. Toschi, N. Musiu, M. Verucchi, F. Prignoli, D. Malatesta, A. F. Jesus, A. Finazzi, F. Amerotti, F. Bagni, E. Mascaro, P. Musso, and M. Bertogna, "er.autopilot 1.1: A software stack for autonomous racing on oval and road course tracks," *IEEE Transactions on Field Robotics*, vol. 1, pp. 332–359, 2024.
4. J. Betz, T. Betz, F. Fent, M. Geisslinger, A. Heilmeier, L. Hermansdorfer, T. Herrmann, S. Huch, P. Karle, M. Lienkamp *et al.*, "TUM autonomous motorsport: An autonomous racing software for the Indy Autonomous Challenge," *J. Field Robot.*, 2023.
5. C. Jung, A. Finazzi, H. Seong, D. Lee, S. Lee, B. Kim, G. Kang, and H. Shim, "Autonomous system for head-to-head race: Design, implementation and analysis; Team KAIST at the Indy Autonomous Challenge," *Field Robotics*, vol. 3, pp. 766–800, 2023.
6. Y. Yu, Y. Liu, F. Fu, S. He, D. Zhu, L. Wang, X. Zhang, and J. Li, "Fast extrinsic calibration for multiple inertial measurement units in visual-inertial system," in *2023 IEEE International Conference on Robotics and Automation (ICRA)*, 2023, pp. 01–07.
7. G. Duran-Martin, M. Altamirano, A. Shestopaloff, L. Sánchez-Betancourt, J. Knoblauch, M. Jones, F.-X. Briol, and K. P. Murphy, "Outlier-robust Kalman filtering through generalised Bayes," in *Proc. 41st ICML*, ser. PMLR, vol. 235, 2024, pp. 12 138–12 171.
8. M. Ester, H.-P. Kriegel, J. Sander, X. Xu *et al.*, "A density-based algorithm for discovering clusters in large spatial databases with noise," in *kdd*, vol. 96, no. 34, 1996, pp. 226–231.
9. E. A. Wan and R. Van Der Merwe, "The unscented kalman filter for nonlinear estimation," in *Proceedings of the IEEE 2000 adaptive systems for signal processing, communications, and control symposium (Cat. No. 00EX373)*. Ieee, 2000, pp. 153–158.
10. R. Rajamani, *Vehicle dynamics and control*. Springer Science & Business Media, 2011.
11. R. Verschuere, G. Frison, D. Kouzoupis, J. Frey, N. van Duijkeren, A. Zanelli, B. Novoselnik, T. Albin, R. Quirynen, and M. Diehl, "acados—a modular open-source framework for fast embedded optimal control," *Math. Program. Comput.*, vol. 14, no. 1, pp. 147–183, 2022.
12. G. Williams, A. Aldrich, and E. A. Theodorou, "Model predictive path integral control: From theory to parallel computation," *J. Guid. Control Dyn.*, vol. 40, no. 2, pp. 344–357, 2017.
13. I. Vizzo, T. Guadagnino, B. Mersch, L. Wiesmann, J. Behley, and C. Stachniss, "KISS-ICP: In Defense of Point-to-Point ICP – Simple, Accurate, and Robust Registration If Done the Right Way," (*RA-L*), vol. 8, no. 2, pp. 1029–1036, 2023.
14. I. S. Mohamed, K. Yin, and L. Liu, "Autonomous navigation of AGVs in unknown cluttered environments: log-MPPI control strategy," *IEEE Robot. Autom. Lett.*, vol. 7, no. 4, 2022.
15. C. Campos, R. Elvira, J. J. Gómez Rodríguez, J. M. M. Montiel, and J. D. Tardós, "ORB-SLAM3: An accurate open-source library for visual, visual-inertial, and multimap SLAM," *IEEE Trans. Robot.*, vol. 37, no. 6, pp. 1874–1890, 2021.